Wiley Analytical Science Virtual Conference

November 9-17

For the 3rd time, The Wiley Analytical Science Conference is back!

It's all happening November 9 - 17

The Wiley Analytical Science Virtual Conference will bring together thousands of researchers and practitioners to share current developments in science and industry. Join for exciting presentations from experts in the fields of analytical and bioanalytical chemistry, pharmaceutical research, materials science, lab automation, and related disciplines.

Register to learn about recent developments & applications in:

- Microscopy
- Spectroscopy
- Mass Spectrometry
- Separation Science
- Much more!

Register here

WILEY

Revisiting Discharge Mechanism of CF$_x$ as a High Energy Density Cathode Material for Lithium Primary Battery
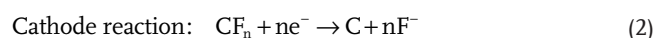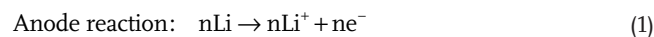
Baharak Sayahpour, Hayley Hirsh, Shuang Bai, Noah B. Schorr, Timothy N. Lambert, Matthew Mayer, Wurigumula Bao, Diyi Cheng, Minghao Zhang, Kevin Leung, Katharine L. Harrison, Weikang Li,* and Ying Shirley Meng*

Lithium/fluorinated graphite (Li/CF$_x$) primary batteries show great promise for applications in a wide range of energy storage systems due to their high energy density (>2100 Wh kg^{-1}) and low self-discharge rate (<0.5% per year at 25 °C). While the electrochemical performance of the CF$_x$ cathode is indeed promising, the discharge reaction mechanism is not thoroughly understood to date. In this article, a multiscale investigation of the CF$_x$ discharge mechanism is performed using a novel cathode structure to minimize the carbon and fluorine additives for precise cathode characterizations. Titration gas chromatography, X-ray diffraction, Raman spectroscopy, X-ray photoelectron spectroscopy, scanning electron microscopy, cross-sectional focused ion beam, high-resolution transmission electron microscopy, and scanning transmission electron microscopy with electron energy loss spectroscopy are utilized to investigate this system. Results show no metallic lithium deposition or intercalation during the discharge reaction. Crystalline lithium fluoride particles uniformly distributed with <10 nm sizes into the CF$_x$ layers, and carbon with lower sp^2 content similar to the hard-carbon structure are the products during discharge. This work deepens the understanding of CF$_x$ as a high energy density cathode material and highlights the need for future investigations on primary battery materials to advance performance.

1. Introduction

Fluorinated graphite (CF$_x$) is a class of cathode materials with the highest theoretical specific energy (>2100 Wh kg^{-1} with theoretical specific capacity of 865 mAh g^{-1} in case of $x = 1$) for lithium primary (non-rechargeable) batteries.[1,2] When using Li metal as the anode material, the primary battery exhibits a low self-discharge rate (<0.5% per year at 25 °C) compared to current alternative chemistries.[1–4] This system, with the proposed governing reaction of CF$_x$ + Li → LiF + C, is one of the leading candidates for a variety of applications where high energy density is required and recharging of the battery is not feasible, e.g., implantable medical devices, military and space applications or other extreme environments.[5] CF$_x$ is a non-stoichiometric compound with $0.5 < x < 1.3$, exhibiting a low electrical conductivity due to the nature of covalent C—F bonds.[1,6] The F/C ratio (x) is shown to be dependent on the synthesis process and structural properties of precursor carbon material (such as coke, graphite, fiber).[6] Ideally, CF$_x$ has a layered structure in which each carbon atom is bonded to three other carbon atoms and one fluorine atom, minimizing the total energy of the structure.[7,8]

The study on possible cathode materials based on fluorides, chlorides, sulfides, etc., initiated in the 1960s, led to the introduction of CF$_x$ as one of the most promising cathode materials in systems based on a lithium anode.[9,10] The first CF$_x$ reaction mechanism was proposed by Watanabe et al.[10–12] with the following steps:

$$\text{Anode reaction:} \quad nLi \rightarrow nLi^+ + ne^- \tag{1}$$

$$\text{Cathode reaction:} \quad CF_n + ne^- \rightarrow C + nF^- \tag{2}$$

B. Sayahpour, S. Bai, D. Cheng, Y. S. Meng
Materials Science and Engineering Program
University of California San Diego
La Jolla, CA 92093-0418, USA
E-mail: shmeng@ucsd.edu
H. Hirsh, M. Mayer, W. Bao, M. Zhang, W. Li, Y. S. Meng
Nano Engineering Department
University of California San Diego
La Jolla, CA 92093-0418, USA
E-mail: wel001@eng.ucsd.edu; shmeng@ucsd.edu

N. B. Schorr, T. N. Lambert
Department of Photovoltaics and Materials Technology
Sandia National Laboratories
Albuquerque, NM 87123, USA
K. Leung
Department of Geochemistry
Sandia National Laboratories
Albuquerque, NM 87123, USA
K. L. Harrison
Nanoscale Sciences Department
Sandia National Laboratories
Albuquerque, NM 87123, USA
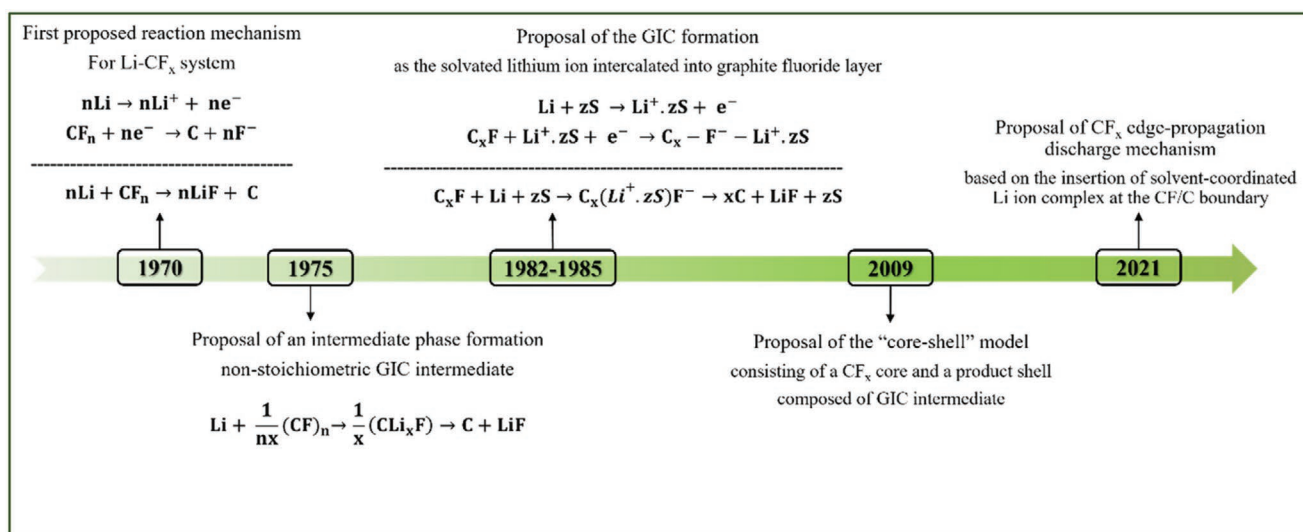
Figure 1. The evolution of the proposed reaction mechanism for Li-CF$_x$ batteries through the years.

Overall cell reaction: $\quad nLi + CF_n \rightarrow nLiF + C$ $\quad\quad$ (3)
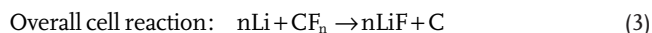
In these studies, it has been suggested that poly-carbon monofluoride was converted into amorphous carbon while crystalline lithium fl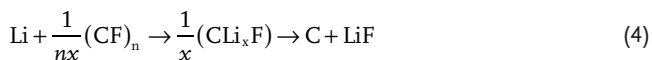uoride (LiF) was formed in the cathode structure during the discharge proce ss. Soon after these studies, in 1975, Whittingham[13] suggested an alternative hypothesis for the overall reaction mechanism as shown below:

$$Li + \frac{1}{nx}(CF)_n \rightarrow \frac{1}{x}(CLi_xF) \rightarrow C + LiF \quad\quad (4)$$

The presence of a non-stoichiometric graphite intercalation compound (GIC) intermediate was proposed to explain the discrepancy between the practical open-circuit voltage ($\approx$2.8 V) from its theoretical value (4.0 V). Through this reaction, an intermediate ternary non-stoichiometric phase as a compound of CLi$_x$F with $x < 1$ was initially suggested, which then disproportionated to form lithium fluoride and graphite. Later, Watanabe et al. investigated the thermodynamic characteristics of CF$_x$ by experimental measurements of entropy and enthalpy, and further confirmed the different values with theoretical calculations.[14–16] They also studied the Gibbs free energies of lithium-ion (Li$^+$) solvation in different solvents,[17] demonstrating that the open-circuit voltage and the voltage plateau increase with higher solvation energies of Li$^+$. Based on these electrochemical results, it has been suggested that the solvent molecules affect the cell reaction and performance of the Li-CF$_x$ cell. Later in the early 1980s, Watanabe et al.[15,17] proposed the following reaction pathway with "S" representative of solvent:

Anode reaction: $Li + zS \rightarrow Li^+ \cdot zS + e^-$ $\quad\quad$ (5)

Cathode reaction: $C_xF + Li^+ \cdot zS + e^- \rightarrow C_x - F^- - Li^+ \cdot zS$ $\quad$ (6)

Overall cell reaction: $C_xF + Li + zS$
$\quad\quad \rightarrow C_x(Li^+ \cdot zS)F^- \rightarrow xC + LiF + zS$ $\quad\quad$ (7)
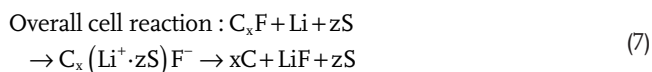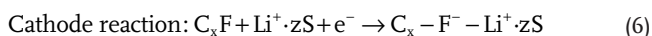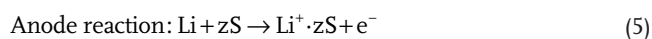
The above mechanism is based on the insertion of the solvated Li$^+$ into CF$_x$ layers to form $C_x(Li^+ \cdot zS)F^-$ (GIC formation), and later, this compound decomposed to carbon, LiF, and solvent, with the solvated discharge product controlling the cathode potential.

This mechanism was generally accepted until 2009 when Read et al.[18] proposed a complementary idea to address the voltage delay in the initial discharge process named as a core–shell model. The authors suggested that the discharge reaction occurs between the CF$_x$ and GIC intermediate phases through a shrinking core model with CF$_x$ as core and a product shell consisting of GIC intermediate, carbon, and lithium fluoride. Most recently, Leung et al.[8] suggested that such solvent-coordinated Li$^+$ complex undergoes an edge-propagation mechanism rather than a bulk-phase reaction pathway. Using density functional theory (DFT) calculations, they demonstrated this discharge mechanism based on lithium insertion at the zigzag edge boundary of the CF$_x$ structure and showed an operating voltage range of 2.5–2.9 V that varied based on electrolyte solvent. This theoretical voltage range was further confirmed by experimental investigations using both solid and liquid state electrolytes in Li-CF$_x$ systems.[19,20] **Figure 1** shows the evolution of the proposed reaction mechanism for Li-CF$_x$ batteries over the years.

Most published studies have mainly relied on the discharge voltage profile and OCV recovery of the Li-CF$_x$ system as the performance criteria with minimal surface and bulk characterizations on the cathode structure or determination of the discharge mechanism due to the sample preparation and air sensitivity of discharge products. Therefore, despite the progress made on this class of cathode material, there is still a lack of understanding of discharge mechanisms and product types. To fully understand the discharge mechanisms in Li-CF$_x$ batteries, the following points need to be thoroughly investigated: (i) the possibility of metallic lithium deposition or intercalation during the discharge reaction, (ii) the type and crystalline structure of the carbon species

**ADVANCED
SCIENCE NEWS**
www.advancedsciencenews.com

**ADVANCED
ENERGY
MATERIALS**
www.advenergymat.de

formed during discharge reaction, and (iii) the size and distribution of formed LiF particles. To provide insights on these main points, we took the following steps to investigate reaction mechanisms in primary lithium systems based on CF_x cathodes in this study. First, a controlled sample preparation method was developed to minimize air exposure given the high reactivity of lithium, lithium compounds, and electrolytes with oxygen and moisture. Second, a cryogenic FIB and STEM setup was utilized to study the size and distribution of discharge products. Using cryogenic electron microscopy enabled us to carefully study the discharge products and avoid possible beam damage to the beam sensitive products as shown by previous studies.[21] Additionally, we designed a novel CF_x cathode electrode with the no extra conductive agent and a non-fluorine-containing binder to investigate the Li-CF_x reaction mechanism precisely. This novel cathode structure, in addition to our custom characterization setups, enabled us to perform a wide range of bulk [Titration gas chromatography (TGC), X-ray diffraction (XRD), Raman spectroscopy, and cryogenic focused ion beam scanning electron microscopy (FIB-SEM) imaging] and surface-sensitive characterizations [X-ray photoelectron spectroscopy (XPS), cryogenic scanning transmission electron microscopy with electron energy loss spectroscopy (Cryo-(S)TEM-EELS)] at different depths of discharge to gain a fuller picture of the Li-CF_x discharge mechanism.
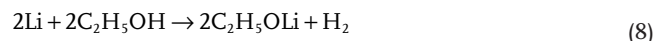
2. Results and Discussion

One of the principal challenges in studying the discharge mechanism in Li-CF_x systems is the presence of carbon and fluorine as dominant elements in various cathode components, e.g., active material, conductive agent, and binder, given the similar and lightweight nature of these elements. To address this, we developed a novel cathode structure with 98 wt% CF_x active material and 2 wt% CMC binder coated on an aluminum mesh. The removal of the carbon conductive additive and fluorine from common binders, such as PVDF or PTFE, minimizes the interference in characterizing the existing fluorine and carbon elements in the CF_x structure and discharge products. The aluminum mesh acts as a conductive network and current collector in the cathode electrode. The electrochemical performance of modified cathode structure compared to a more conventional cathode structure is presented in Figure S1, Section S1 (Supporting Information). More details on this cathode and the coin-cell specifications used in sample preparations are provided in Table S1 (Supporting Information).

2.1. Evaluating Possible Metallic/Intercalated Lithium after Discharge

Our group has recently demonstrated the TGC technique as an effective method to quantify metallic/intercalated lithium.[22] Given that the reaction of Li^0 (metallic) or Li_xC_6 (intercalated) with ethanol solvent (Equations (8) and (9)) leads to H_2 gas evolution, we can apply the TGC technique

to evaluate possible metallic or intercalated lithium in a discharged CF_x cathode.

$$2Li + 2C_2H_5OH \rightarrow 2C_2H_5OLi + H_2 \tag{8}$$

$$2Li_xC_6 + 2xC_2H_5OH \rightarrow 2C_6 \left(graphite\right) + 2xC_2H_5OLi + xH_2 \tag{9}$$

The absence of detected H_2 above the background levels, as seen in Figure S2 (Supporting Information), indicates no metallic or intercalated lithium in the system. The details of the TGC method are presented in Section S2 (Supporting Information). We further evaluated this observation using galvanostatic cycling of Li-CF_x at a lower discharge voltage range (down to 0.001 V) and attempted recharge to understand the possible voltage plateaus for lithium (de)intercalation into graphitic layers.[23,24] The electrochemical performance of the Li-CF_x cell is presented in Figure S3, Section S3 (Supporting Information). The voltage profile of the system during the charging process started at and continued with a steep curve, with no plateau observed at low voltages. This confirms the absence of any lithium deposition or intercalation, and the resulting charging is likely purely capacitive in nature. Interestingly, the electrochemical performance of the Li-CF_x during discharge and consequently charge show that the CF_x structure acts similar to the hard carbon structure reported in the literature.[25] This suggests the transformation of CF_x structure to hard-carbon type structure at discharge state to 1.5 V.

2.2. Investigating the Type and Crystalline Structure of Carbon

To investigate the type and crystalline structure of the formed carbon species, we evaluated the formation of the products through various depths of discharge (DoD) using XRD and Raman spectroscopy. **Figure 2**b presents XRD results from pristine to discharged (to 1.5 V) samples. Our results confirm crystalline LiF (Fm-3m) as the main product at the beginning of the discharge, in line with the previous reports.[26,27] An important point that was not considered in previous reports[27–30] is the overlap of the crystalline LiF (Fm-3m) peak with the dominant form of Al (Fm-3m). To address this here, the XRD measurement was directly performed on the cathode powder without aluminum mesh. CF_x peaks at 7° and 18° were observed in the pristine sample with no evident change up to 10% DoD. The presence of CF_x in the early stages of discharge when LiF begins to form can imply the possibility of starting the reaction from the edges and surface of the CF_x particles, preserving the overall bulk CF_x structure. This observation is consistent with previous computational work by Leung et al. proposing the edge-propagation mechanism in Li-CF_x system.[8] CF_x peaks started to disappear after 40% DoD, while the presence of a graphitic peak at around 9° remained through discharged to 1.5 V state. This result confirmed the presence of both the graphitic and amorphous characteristics of CF_x materials and is in good agreement with previous computational work by Goddard et al.[7] It should also be noted that no intermediate phases were detected in our ex situ XRD measurement, which
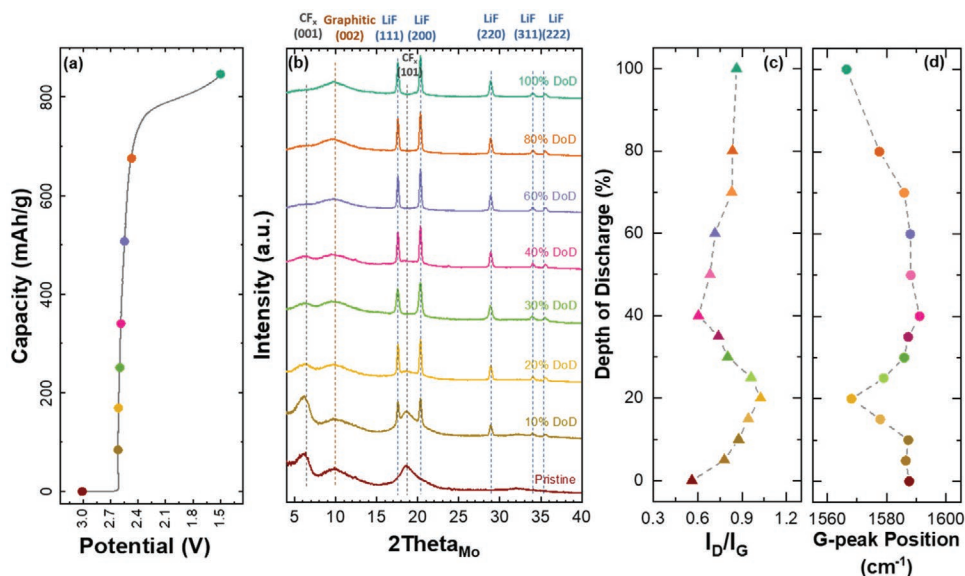
Figure 2. Ex situ X-ray diffraction (XRD) and Raman spectroscopy on CF_x cathodes [CF_x:CMC (98:2 wt%)]. a) The electrochemical performance of the Li-CF_x system through different depths of discharge. b) Ex situ XRD results on CF_x cathode at different depths of discharge (DoD). c) The ratio of D-band over G-band (I_D/I_G) and d) The G-peak position (cm^{-1}) from ex situ Raman spectra.

is consistent with the previous reports.[27,29] More details on XRD measurements are provided in Figure S4, Section S4 (Supporting Information).

Raman spectroscopy was also performed using the modified cathode structure at different depths of discharge to better understand the nature of carbon species in the system (Figure 2c,d and Figure S5, Supporting Information). The G-band ($\approx$1580 cm^{-1}) is the characteristic peak of graphitic carbon representative of the stretching mode of C–C sp^2 species,[31,32] while the D-band ($\approx$1350 cm^{-1}) is linked to breathing modes of carbon rings and requires defects in the carbon structure to materialize.[31,32] The ratio of the D-band to G-band peaks (I_D/I_G) has been previously used to quantify the extent of disordering as well as sp^2 content in CF_x structures.[31,33] A smaller I_D/I_G ratio is attributed to a higher degree of sp^2 in the structure[31,33] and also lower disordering and defects in graphitic layers.[32,34] In our measurements, the I_D/I_G began around 0.55 and increased to 1.1 through 20% DoD, and then decreased through 20–40% DoD back to about 0.6. Again, after 40% DoD, this ratio increased with a lower ratio to around 0.9. The overall increasing trend is not severe.[32] Furthermore, the absence of doublets on G peaks suggests no staging process of lithium intercalation into the carbon structure.[35–37] This observation complements our results from TGC and the electrochemical performance measurements. Previously, Ferrari et al. observed a reversed correlation between I_D/I_G ratio and G-peak position based on experimental results.[31,38] G-peak position is susceptible to lattice parameter changes, possibly caused by chemical structure transformation during discharge.[36,37] We observed that the I_D/I_G initially increased through 20% DoD due to the lithium-ion insertion into the CF_x layers and the consequent expansion. Together, the G-peak position initially shifted to lower wavenumbers through 20% DoD due to the CF_x reacting with lithium to form the C–C bonds with lower energy. This phenomenon can also be further observed in the narrowing

of G-peak in this region, as shown in Figure S6b (Supporting Information). The G-peak position then blueshifted up to 40% DoD. This shift can be attributed to the increase of the force constants of the in-plane C–C bonds by solvent insertion into CF_x structure and the continued formation of LiF, which can also be seen in the widening of G-peak in this region.[37] Later, this shift moved to lower wavenumbers through the discharge to 1.5 V, indicating continuation of Li-ion reaction with CF_x throughout the layers leading to the accumulation of LiF and lower energy C–C bonds.

A combination of XRD, Raman spectroscopy, and electrochemical performance provides a comprehensive understanding of the carbon species formed during discharge reactions. Overall, the increasing trend in I_D/I_G and the decreasing trend in the G-peak position show a lower sp^2 content of carbon in the discharged cathode than the pristine cathode.

2.3. Inspecting the Size and Distribution of LiF

To understand the surface chemistry of the CF_x cathode throughout the discharge reaction, we performed XPS on carbon (C), fluorine (F), lithium (Li), and oxygen (O) core levels, as shown in **Figure 3**. The survey spectra presented in Figure S7, Section S6 (Supporting Information) show no other elements in the system, indicating no contamination or impurities in the samples. The pristine sample shows C–F bonding in both C and F regions with no signal in the Li region. We observed a decrease in C–F and an increase in C–C/C–H components as CF_x decomposed through depths of discharge. The ratio of C–F/C–C components decreased as the cell progressed to deeper discharge stages. Consistent with XRD data, the intensity of C–F spectra from XPS significantly decreased after 30% DoD and C–C remained through discharge to the 1.5 V state that corresponds with the formation of carbon products.
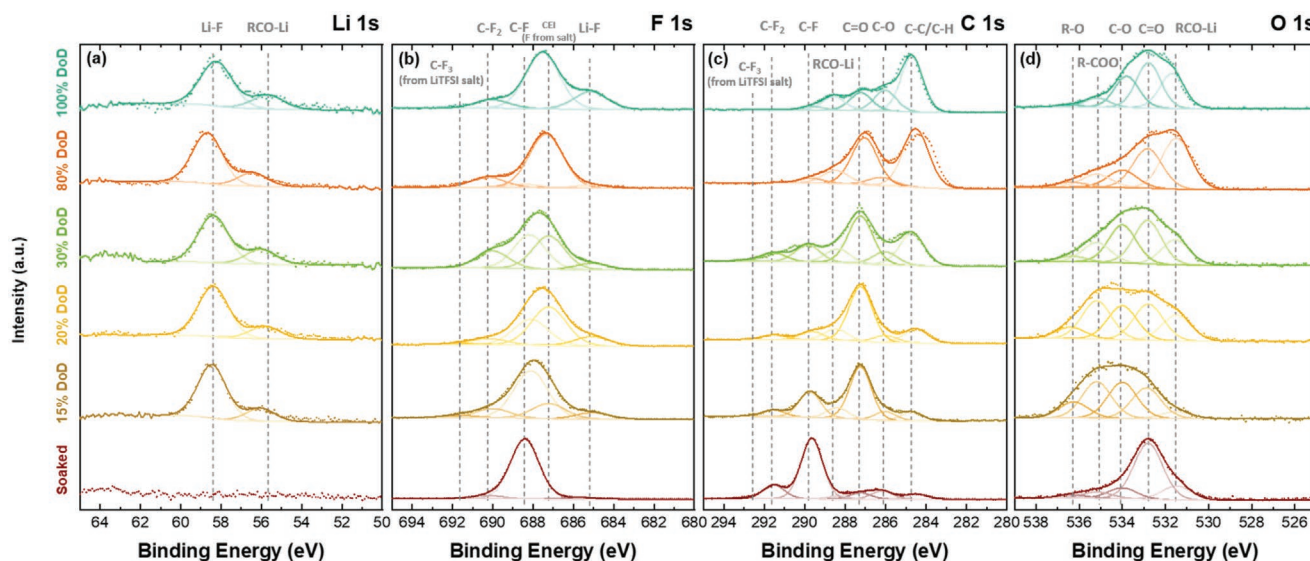
Figure 3. X-ray photoelectron spectroscopy (XPS) on CF_x cathodes [CF_x:CMC (98:2 wt%)] at different depths of discharge (DoD). The data is shown in different regions of a) Li 1s; b) F 1s; c) C 1s; and d) O 1s.

Meanwhile, we observed the formation of LiF and cathode electrolyte interphase (CEI) components. XPS results show that CEI consists of C–O, C=O, R–CO–Li, and R–COO species that mainly form in the range of 20% to 40% DoD. LiF formation shows a low intensity and a minimal growth through depths of discharge, suggesting a limited formation of LiF on the surface and the possibility of LiF formation between the CF_x layers. We also performed a control experiment on the discharged to 1.5 V sample with two types of washed and unwashed samples. The results presented in Figure S8, Section 6 (Supporting Information) demonstrated a minimal change in the amount of LiF on the surface of the washed and unwashed electrodes, further

confirming the hypothesis that the LiF particles are limited on the electrode surface.

Previous studies reported LiF products of spherical, cubic, or random morphology with the sizes of 100–600 nm on the surface of the CF_x particles demonstrated by SEM.[27,29,39–41] A critical point to consider here is the possibility of air exposure and formation of other products such as lithium oxide (Li_2O) and lithium carbonate (Li_2CO_3) with similar spherical or cubic shapes.[42,43] While overlooked in most previous studies, it is vital to implement chemical mapping on the cathode surface to distinguish the products formed during discharge reactions from those formed by air contamination. Here, we performed cross-sectional FIB and SEM to check the size and morphology of LiF particles formed during the discharge reaction. SEM and cross-sectional FIB-SEM images along with elemental mappings for the pristine and discharged CF_x cathodes without air exposure are presented in Figures S9 and S10, Section 7 (Supporting Information). The pristine CF_x powder shows a dense layered structure with nearly parallel layers. After discharge, no spherical or cubic LiF particles were observed in the cross-sectional images. However, the layered CF_x structure clearly changed to a more disordered structure. This change is likely due to the –F removal from the surface and possibly the accumulation of LiF between the layers. Earlier studies suggested a possible volume expansion after discharge in other primary batteries.[21,39] To better understand this, we further evaluated the thickness change of the cathode electrode through various depths of discharge using cross-sectional imaging and operando dilatometry. The cross-sectional SEM images showed a volume expansion of the cathode electrode after discharge. The cross-sectional SEM images of the cathode electrode for the pristine and discharged cathodes are shown in **Figure 4**a,b. More images are provided in Figure S11, Section S8 (Supporting Information). About two times volume expansion was observed due to the LiF and CEI formations. Operando electrochemical dilatometry technique was utilized to evaluate the vertical
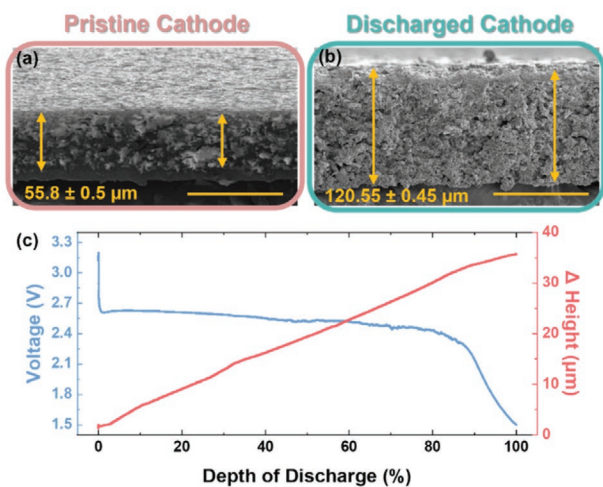

Figure 4. The scanning electron microscopy (SEM) images and operando dilatometry measurement show two times volume expansion after discharge to 1.5 V. The cross-sectional SEM images of the cathode electrodes for a) the pristine; and b) The discharged (to 1.5 V) cathodes [CF_x: C65: PVDF (80:10:10) wt%]. The scale bars are 100 μm. c) The operando dilatometry measurement results of a cathode [CF_x: C65: PVDF (80:10:10) wt%].

**ADVANCED
SCIENCE NEWS**

www.advancedsciencenews.com

**ADVANCED
ENERGY
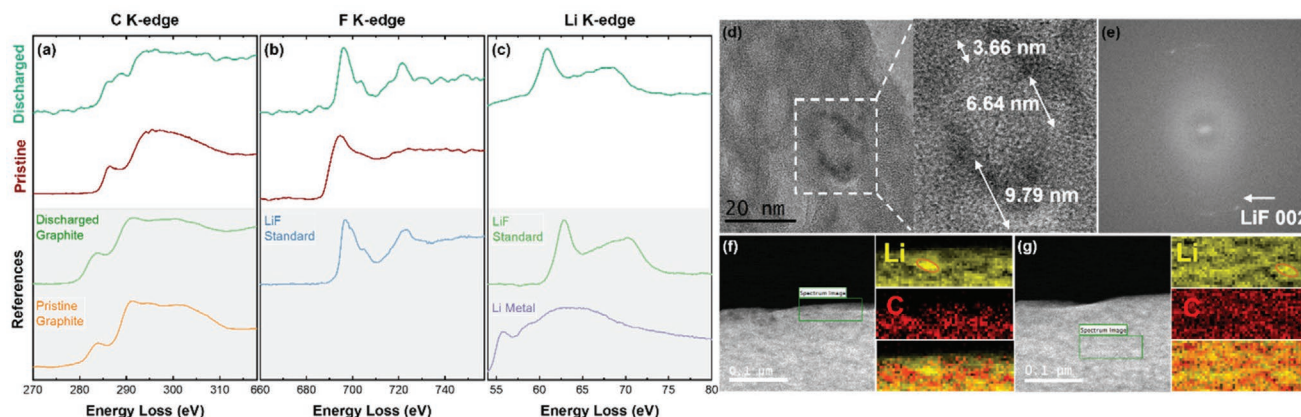MATERIALS**

www.advenergymat.de

Figure 5. Cryogenic scanning transmission electron microscopy (Cryo-STEM) and electron energy loss spectroscopy (EELS) mapping. The EELS data on pristine and discharged cathode samples [CF_x:CMC (98:2 wt.%)] in a) C K-edge region compared to pristine and discharged graphite; b) F K-edge region compared to LiF standard; and c) Li K-edge region compared to Li metal and LiF standard; d) Cryo-HRTEM on the discharged sample [CF_x : CMC (98:2 wt%)]; e) The fast Fourier transform (FFT) showing LiF. EELS elemental mapping on f) the surface of the sample; and g) the bulk of the sample in Li and C regions.

dimensional changes in the CF_x cathode electrode during the discharge without cell disassembly. The result is presented in Figure 4c, and the detailed information is provided in Section S9 (Supporting Information). This operando measurement demonstrates a change of CF_x electrode thickness from 33 µm to about 67 µm after discharge, corresponding to a ≈203% increase in height during discharge. Evaluating the 1st derivation of the thickness change shows two minima around 20% and 40% depths of discharge which indicate major changes of the reaction mechanism in these points.

While cross-sectional SEM and operando dilatometry provide useful insights on the cathode volume expansion due to products and CEI formation, it provides limited information on the nature of the species responsible for this expansion. To thoroughly investigate this, we utilized the Cryo-(S)TEM-EELS on the discharged CF_x cathode. Cryogenic techniques minimize the possible impact on the morphology and chemical structure of the particles from the beam.[44] STEM-EELS was performed on pristine and discharged (1.5 V) electrodes. The EELS spectra of C K-edge, F K-edge, and Li K-edge are compared with reference samples in **Figure 5**a–c. The C K-edge of the pristine electrode exhibits an amorphous carbon structure similar to the previously reported data in the literature.[45] Upon discharge to 1.5 V, the signal in C K-edge shows a combination of amorphous and graphitic structures. This observation for carbon is well aligned with our XRD data, where a broad graphitic peak (002) at 9° was observed through different depths of discharge. No lithium signal was detected in pristine cathode electrodes, while in the discharged samples, the newly formed LiF was identified in both F K-edge and Li K-edge regions in line with the characteristic peaks of the LiF reference sample. The EELS data also show no metallic lithium on cathode electrodes, confirming our previous TGC, Raman spectroscopy, and electrochemical performance tests.

We performed EELS mapping to further elucidate the distribution and size of LiF particles on lamella samples prepared by the Cryo-FIB lift-out method previously developed in our group.[46] The EDS images and the details of sample prepara-

tion are presented in Figure S13 and Section S10 (Supporting Information). The fast Fourier transform (FFT) further confirms crystalline LiF as the reaction product. The distribution of LiF particles was investigated using inverse FFT analysis, which shows a particle size of less than 10 nm. This observation was also verified by the EELS mapping conducted on the surface and bulk of the electrode. The EELS elemental mapping on the surface and the bulk of the sample in Li and C regions are presented in Figure 5, while F region is shown in Figure S14 (Supporting Information) in a well alignment with Li. The EELS mappings show the enhanced signal for Li in random locations as a representative of LiF particles with sizes smaller than 10 nm. It is important to note that this is the first direct observation of LiF particle size and distribution on a CF_x electrode ever reported in the literature. The LiF particles were observed on the layers of formed carbon. We found no evidence of aggregation of LiF particles on the surface or outside of the carbon layers. This observation implies a limited movement of fluorine ions during the discharge while the Li ions were traveling through the layers.

2.4. Three-Region Discharge Mechanism in Li-CF_x Systems

Based on the findings presented here, we propose a three-region discharge mechanism in Li-CF_x systems: (I) beginning the discharge process up to 20% depth of discharge, the lithium ions start to react with CF_x and form LiF. The formation of LiF and the presence of the CF_x structure were observed in XRD and XPS results in this initial stage. XPS results also showed that the CEI starts to form in this region. The lithium-ion insertion and defluorination of the CF_x particles due to the LiF formation can be the main reason for the increase in I_D/I_G ratio and decrease in G-peak position in Raman spectroscopy results. (II) In the range of 20–40% depth of discharge, lithium ions continue to react with CF_x resulting in the transformation of CF_x structure to more carbon formation. These points were clearly shown by considerable reduction of CF_x peaks
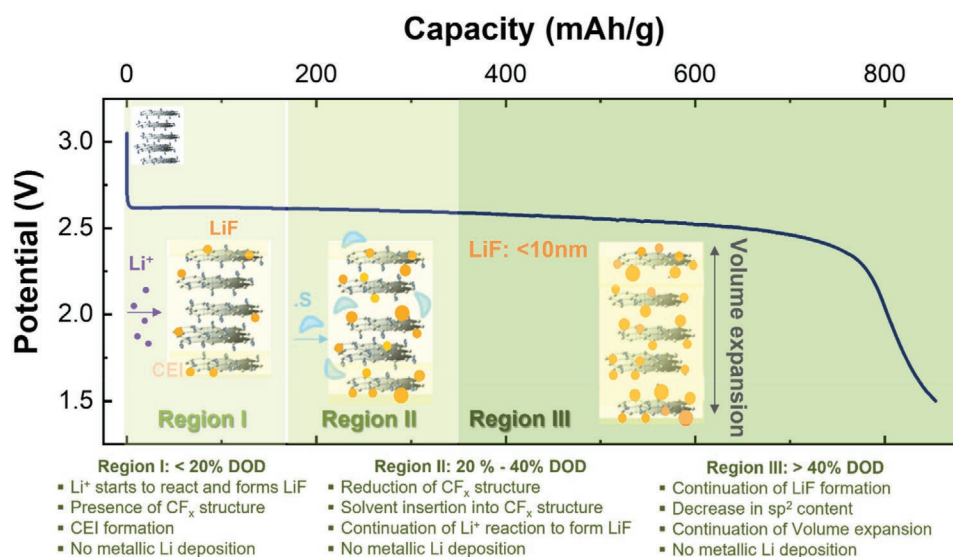
ADVANCED
SCIENCE NEWS
www.advancedsciencenews.com

ADVANCED
ENERGY
MATERIALS
www.advenergymat.de

Figure 6. The schematic of the Li-CF_x system mechanism through the depth of discharge.

in XRD as well as reduction of C–F bond and increasing of C–C bond in XPS results in this region. Solvent insertion into CF_x structure is also observed in this region, with a decrease in I_D/I_G ratio and an increase in G-peak position and FWHM bandwidth in the Raman spectroscopy results. XPS results also showed that the CEI mainly grows in this region. (III) Above 40% depth of discharge to the discharged to 1.5 V state, LiF particles continue to form, but no change in the graphitic carbon was observed. There is about two times volume expansion in the cathode electrode through the discharge process shown by cross-sectional SEM images and operando dilatometry measurement. No metallic or intercalated lithium was observed at discharge to 1.5 V. **Figure 6** summarizes the three-step model mentioned above.

3. Conclusions

In this work, a CF_x cathode electrode with minimal carbon and fluorine additives was developed for a precise study of the Li-CF_x discharge mechanism. We demonstrated that: (i) There is no lithium deposition or intercalation through the entire discharge. This was shown with TGC, Raman spectroscopy, STEM-EELS, and electrochemical performance tests. (ii) The CF_x structure transforms to a hard-carbon like structure with less sp^2 content by increasing depth of discharge, as shown by XRD, Raman spectroscopy, STEM-EELS, and the electrochemical performance tests. (iii) The crystalline LiF particles, detected by XRD and XPS, uniformly covered the layers of CF_x structure as shown by Cryo-(S)TEM-EELS, and the LiF has a size range of < 10 nm throughout the CF_x layers. A three-step discharge reaction mechanism is proposed in agreement with our electrochemical performances. This multiscale discharge mechanism study will play an important role in future experimental and computational works toward designing a higher power density cathode and help pave the path for developing a rechargeable Li-CF_x battery.

4. Experimental Section

Electrochemical Tests: All the electrochemical performances were tested using CR2032 coin cells. The cathode electrodes consisted of pristine CF_x powder (ACS Materials, F/C ratio-1.05) as the active material and carboxymethyl cellulose (CMC) (Sigma-Aldrich) as the F-free binder with the ratio of 98:2 wt% coated on aluminum mesh (MTI). 50 μL of 0.5 м Lithium bis(trifluoromethanesulfonyl)imide (LiTFSI) in propylene carbonate (PC): dimethoxyethane (DME) (1:4, v:v) electrolyte was used with pure Li chip (1 mm thickness) as the anode. This modified cathode structure was used for all characterization techniques unless otherwise noted. The current rate was 10 mA g^{-1} with cathode loading of ≈3.5 ± 0.5 mg cm^{-2}. 1.5 V was used as the cut-off voltage with an 8 h rest at the beginning of the program. Detailed summary information of the coin-cell testing specifications is presented in Table S1, Section S1 (Supporting Information).

X-Ray Diffraction (XRD): The XRD measurements were done by a Bruker APEX II Ultra diffractometer with Mo Kα ($\lambda = 0.71073$ Å) radiations to check the crystal structures. The diffraction images gathered by the 2D detector within an angular range of 4° to 40° were merged and integrated with DIFFRAC.EVA (Bruker, 2018) to produce 2d-plots. The samples were prepared by scratching the cathode electrode and filling the capillary tubes inside an Ar-filled glovebox with < 0.1 ppm H_2O level. The cathode samples were not washed before these measurements.

Scanning Electron Microscopy (SEM): A FEI Apreo scanning electron microscope was used for cross-sectional imaging on the cathode electrodes. The standard mode with ETD detector using 0.1 nA and 2 kV was utilized in these imaging tests. The samples were not washed before these tests and were prepared inside an Ar-filled glovebox with < 0.1 ppm H_2O level.

Raman Spectroscopy: Raman spectroscopy was performed using Renishaw inVia Raman Microscope. The samples were sealed between two thin transparent glass slides inside an Ar-filled glovebox with < 0.1 ppm H_2O level. The measurements were run using a 532 nm laser source, 1800 L mm^{-1} grating, and ×20 magnification.

X-Ray Photoelectron Spectroscopy (XPS): XPS was performed using an AXIS Supra by Kratos Analytica. XPS electrode samples were disassembled and prepared inside an Ar-filled glovebox with < 0.1 ppm H_2O level. Unwashed samples were directly dried under vacuum before measurements. The washed samples were rinsed with PC solvent before this procedure. The XPS was operated using an Al anode source at 15 kV, scanning with a step size of 0.1 eV and 200 ms dwell time. Fits of the XPS spectra were performed with CasaXPS software to identify the chemical composition on the surface of the electrodes.

Dilatometry Measurement: An EL-CELL electrochemical dilatometer ECD-3-nano was used for measuring height changes during the discharge of a CF_x cathode. The instrument has a < 5 nm resolution with a total range of 250 μm, within the maximum cathode thickness and height changes. Measurements were made with a three-electrode configuration. The CF_x cathode [CF_x: Carbon C65: PVDF (80:10:10) wt%] was punched into a 10 mm diameter disk and assembled into the dilatometer. A 12 mm diameter Lithium metal disk (750 μm thick) was used as an anode and a separate piece of lithium was connected to serve as the reference. ≈500 μL of 0.5 M LiTFSI in PC: DME (1:4, v:v) was used to fill the dilatometer. Assembly and filling of the dilatometer were undertaken within an Ar filled mBraun glovebox with < 0.1 ppm O_2 and H_2O. After a 20 h rest the cathode was discharged at 10 mA g^{-1} until the 1.5 V cut-off was reached with height displacements measured every 30 s throughout this period.

Titration Gas Chromatography (TGC): TGC was performed using a Shimadzu GC instrument equipped with a BID detector and using an ultra-high purity Helium (99.999%) as the carrier gas. The samples were prepared in an Ar-filled glovebox with less than 0.1 ppm moisture level. Each sample was immediately transferred to a glass flask after disassembling and sealed using a septum under Ar. A 0.5 mL of ethanol was injected into the container to fully react with metallic lithium. After reaction completion, a 30 μL gas sample was taken from the container using a gastight Hamilton syringe and immediately injected into the GC. The amount of metallic lithium was quantified based on the amount of detected H_2 gas by the GC.

Cryogenic Focused Ion Beam (Cryo-FIB): The FIB-SEM was conducted on the FEI Scios Dual-beam microscopy; the discharged cells were disassembled in the Ar-filled glovebox after cycling. The samples were transferred to the FIB chamber via quick loader without any exposure to air. The electron beam operating voltage was 5 kV, and the stage was cooled with liquid nitrogen to −180 °C or below. Sample cross-sections were exposed using a 1 nA ion beam current and cleaned at 0.1 nA.

Scanning Transmission Electron Microscopy–Electron Energy Loss Spectroscopy (STEM–EELS): The lift-out sample from the FIB chamber was transferred to an Ar-filled glovebox using an air-free quick loader (FEI). The lamella was mounted to a vacuum cooling holder (Mel-build) to eliminate air exposure and transferred to the TEM column directly. HRTEM/STEM/EELS results for discharged samples were obtained on ThermoFisher Talos X200 equipped with a Gatan Oneview camera operated at 200 kV and UltraFast DualEELS Spectrum Imaging detector. The image was acquired with minimum beam damage at spot size 6 with a dose rate of 200 electrons Å^{-2}*s. The EELS spectrum and mapping were collected with an exposure time of 0.02 s, and the dispersion energy was 0.25 eV per channel.

Supporting Information

Supporting Information is available from the Wiley Online Library or from the author.

Conflict of Interest

The authors declare no conflict of interest.

Author Contributions

B.S. and Y.S.M. conceived the idea. B.S., M.M., and W.L. designed the experiments. B.S. performed and processed the data for SEM, XRD, and Raman spectroscopy. W.L. performed and processed the data for XPS. B.S., W.B., and W.L. performed and processed the data for TGC. N.S., T.L. K.L., and K.H. designed, performed, and processed the data for dilatometry measurement. W.L. and D.C. performed Cryo-FIB for sample preparation. S.B. and M.Z. performed and processed the data for STEM-EELS. All authors discussed the results and contributed to the manuscript. All authors have approved the final version of the manuscript.

Data Availability Statement

The data that support the findings of this study are available from the corresponding author upon reasonable request.

[1] Q. Zhang, K. J. Takeuchi, E. S. Takeuchi, A. C. Marschilok, *Phys. Chem. Chem. Phys.* **2015**, *17*, 22504.

[2] D. Linden, T. B. Reddy, *Handbook of Batteries*, McGraw-Hill Books, **2001**.

[3] R. L. Higgins, L. R. Erisman, Applications of the Lithium/Carbon Monofluoride Battery, in *Proc. 28th Power Sources Symposium*, Electrochemical Society, Atlantic City, NJ **1978**.

**ADVANCED
SCIENCE NEWS**

www.advancedsciencenews.com

**ADVANCED
ENERGY
MATERIALS**

www.advenergymat.de

[4] D. C. Bock, A. C. Marschilok, K. J. Takeuchi, E. S. Takeuchi, *Electrochim. Acta* **2012**, *84*, 155.

[5] D. Linden, T. Reddy, *Handbook of Batteries*, 3rd ed., McGraw Hill, **2002**.

[6] N. Watanabe, T. Nakajima, H. Touhara, *Graphite Fluorides*, Elsevier, Japan **1988**.

[7] S. S. Han, T. H. Yu, B. V. Merinov, A. C. T. van Duin, R. Yazami, W. A. Goddard, III, *Chem. Mater.* **2010**, *22*, 2142.

[8] K. Leung, N. B. Schorr, M. Mayer, T. N. Lambert, Y. S. Meng, K. L. Harrison, *Chem. Mater.* **2021**, *33*, 1760.

[9] T. Nakajima, *Lithium-Graphite Fluoride Battery-History and Fundamentals*, Elsevier, Japan **2017**, pp. 305–323.

[10] N. Watanabe, M. Fukuda, *US Patent US3536532A, Primary Cell for Electric Batteries* **1970**.

[11] M. Fukuda, T. Iijima, in *Extended Abstract No. 41*, The Electrochemical Society Fall Meeting, Cleveland, OH **1971**, p. 100.

[12] N. Watanabe, M. Takashima, *Proc. of the 7th Int. Symp on Fluorine Chemistry*, ISFC, Santa Cruz, CA **1973**, p. 19.

[13] M. S. Whittingham, *J. Electrochem. Soc.* **1975**, *122*, 526.

[14] K. Ueno, N. Watanabe, T. Nakajima, *J. Fluorine Chem.* **1982**, *19*, 323.

[15] N. Watanabe, T. Nakajima, R. Hagiwara, *J. Power Sources* **1987**, *20*, 87.

[16] J. L. Wood, A. J. Valerga, R. B. Badachhape, J. L. Margrave, *R&D Tech. Report: ECOM-0105-F; Contract DAAB 07-72-C-0105*, **1972**.

[17] N. Watanabe, R. Hagiwara, T. Nakajima, H. Touhara, K. Ueno, *Electrochim. Acta* **1982**, *27*, 1615.

[18] S. S. Zhang, D. Foster, J. Wolfenstine, J. Read, *J. Power Sources* **2009**, *187*, 233.

[19] Z. Ding, C. Yang, J. Zou, S. Chen, K. Qu, X. Ma, J. Zhang, J. Lu, W. Wei, P. Gao, L. Wang, *Adv. Mater.* **2021**, *33*, 2006118.

[20] C. Pang, F. Ding, W. Sun, J. Liu, M. Hao, Y. Wang, X. Liu, Q. Xu, *Electrochim. Acta* **2015**, *174*, 230.

[21] C. Jiang, B. Wang, Z. Wu, J. Qiu, Z. Ding, J. Zou, S. Chen, P. Gao, X. Niu, L. Wang, H. Li, *Nano Energy* **2020**, *70*, 104552.

[22] C. Fang, J. Li, M. Zhang, Y. Zhang, F. Yang, J. Z. Lee, M.-H. Lee, J. Alvarado, M. A. Schroeder, Y. Yang, B. Lu, N. Williams, M. Ceja, L. Yang, M. Cai, J. Gu, K. Xu, X. Wang, Y. S. Meng, *Nature* **2019**, *572*, 511.

[23] J. O. Besenhard, *Handbook of Battery Materials*, Wiley-VCH Verlag GmbH, Austria **1999**.

[24] J. Asenbauer, T. Eisenmann, M. Kuenzel, A. Kazzazi, Z. Chen, D. Bresser, *Sustainable Energy Fuels* **2020**, *4*, 5387.

[25] N. Wang, Q. Liu, B. Sun, J. Gu, B. Yu, W. Zhang, D. Zhang, *Sci. Rep.* **2018**, *8*, 1.

[26] K. Guérin, M. Dubois, A. Hamwi, *J. Phys. Chem. Solids* **2006**, *67*, 1173.

[27] G. Zhong, H. Chen, Y. Cheng, L. Meng, H. Liu, Z. Liu, G. Zheng, Y. Xiang, X. Liu, Q. Li, Q. Zhang, H. Yue, C. Lu, Y. Yang, *J. Mater. Chem. A* **2019**, *7*, 19793.

[28] Y. R. Li, A. M. Bruck, A. B. Brady, D. Bock, K. J. Takeuchi, E. S. Takeuchi, A. C. Marschilok, *J. Electrochem. Soc.* **2017**, *164*, A2457.

[29] Y. Ahmad, K. Guérin, M. Dubois, W. Zhang, A. Hamwi, *Electrochim. Acta* **2013**, *114*, 142.

[30] M. A. Rodriguez, M. R. Keenan, G. Nagasubramanian, *J. Appl. Crystallogr.* **2007**, *40*, 1097.

[31] D. Hai-Yang, W. Li-Wu, J. Hui, H. Ning-Kang, *Chin. Phys. Lett.* **2007**, *24*, 2122.

[32] I. Childres, L. A. Jauregui, W. Park, H. Caoa, Y. P. Chena, *New Developments in Photon and Materials Research*, Nova Science Publishers, Inc., New York **2013**, pp. 403–418.

[33] A. Ferrari, J. Robertson, *Phys. Rev. B: Condens. Matter Mater. Phys.* **2000**, *61*, 14095.

[34] M. I.n Inaba, *J. Electrochem. Soc.* **1995**, *142*, 20.

[35] R. Fong, U. von Sacken, J. R. Dahn, *J. Electrochem. Soc.* **1990**, *137*, 2009.

[36] V. Stancovski, S. Badilescu, *J. Appl. Electrochem.* **2014**, *44*, 23.

[37] C. Sole, N. E. Drewett, L. J. Hardwick, *Faraday Discuss.* **2014**, *172*, 223.

[38] A. C. Ferrari, *Diamond Relat. Mater.* **2002**, *11*, 1053.

[39] J. Read, E. Collins, B. Piekarski, S. Zhang, *J. Electrochem. Soc.* **2011**, *158*, A504.

[40] M. Mar, Y. Ahmad, K. Guérin, M. Dubois, N. Batisse, *Electrochim. Acta* **2017**, *227*, 18.

[41] J. H. S. R. Desilva, R. Vazquez, P. E. Stallworth, T. B. Reddy, J. M. Lehnes, R. Guo, H. Gan, B. C. Muffoletto, S. G. Greenbaum, *J. Power Sources* **2011**, *196*, 5659.

[42] L. O. Nanoparticles, *Schmierungstechnik* **1988**, *19*, 61.

[43] N. Chen, E. Zhou, D. p. Duan, X. m. Yang, *Korean J. Chem. Eng.* **2017**, *34*, 2748.

[44] J. Z. Lee, T. A. Wynn, M. A. Schroeder, J. Alvarado, X. Wang, K. Xu, Y. S. Meng, *ACS Energy Lett.* **2019**, *4*, 489.

[45] F. Langenhorst, V. L. Solozhenko, *Phys. Chem. Chem. Phys.* **2002**, *4*, 5183.

[46] D. Cheng, T. A. Wynn, X. Wang, B. Lu, S. J. Kim, Y. S. Meng, *Joule* **2020**, *4*, 2484.